Title: Stretching of the insect mechanoreceptor evokes mechano-electrical transduction in auditory chordotonal neurons

Authors: Atitheb Chaiyasitdhi[1], Manuela Nowotny[2], Marcel Van der Heijden[3], and Benjamin Warren[4]

Author affiliations:

[1]Department of Genetics, Genomics, and Cancer Sciences, University of Leicester, Leicester, United Kingdom.

[2]Institute for Zoology and Evolutionary Research, Friedrich Schiller University, Jena, Germany.

[3]Department of Neuroscience, Erasmus Medisch Centrum Rotterdam, Rotterdam, the Netherlands.

[4]School of Life Sciences, Keele University, Newcastle, United Kingdom.

Corresponding author: b.warren@keele.ac.uk

ABSTRACT

Insect proprioception, vibration and sound detection rely on the scolopidium—a mechanosensory unit enclosing the sensory cilium of chordotonal organ neurons. The cilium contains mechanosensitive ion channels, and is enclosed by a scolopale cell with its tip embedded in a cap. Despite knowledge of the scolopidium's structure in multiple insects, the mechanism by which mechanical force elicits the transduction current remains speculative. We examined scolopidia in the auditory Müller's organ of the desert locust and present a comprehensive three-dimensional ultrastructure of a scolopidium using Focused Ion Beam Scanning Electron Microscopy (FIB-SEM). Next, we characterised sound-evoked motions of Müller's organ and the scolopidium using Optical Coherence Tomography (OCT) and high-speed light microscopy. We further measured transduction currents via patch clamp electrophysiology during mechanical stimulation of individual scolopidia. By combining ultrastructure, sound-evoked motions, and transduction current recordings, our finding suggests that the scolopidium is activated best by stretch along the ciliary axis.

30 **MAIN TEXT**

31 ## 1. Introduction

32 All animal ears share the same fundamental purpose of converting sound-evoked vibrations
33 into electrical signals[1]. In insects, this process, known as mechano-electrical transduction
34 (MET), occurs in the distal ciliated endings of chordotonal organ neurons[2]. The cilium is
35 enclosed in an evolutionarily conserved structure, the scolopidium[3], where it extends into a
36 receptor lymph cavity made by the scolopale cell. The ciliary tip is embedded in an extracellular
37 cap tightly fused to an attachment cell. This stereotypical structure of a scolopidium is found
38 in all insect chordotonal organs and underlies proprioception, vibration and sound detection[4].
39 Thus, understanding how the scolopidium functions has widespread implications for insect
40 behaviour.

41 While it is established that MET takes place within the cilium, the precise mechanism
42 remains speculative[4]. MET channels open in response to mechanical stimulation leading to a
43 depolarisation that triggers downstream spikes. Putative transduction channels, No
44 mechanoreceptor potential C (NompC) and Nanchung-Inactive (Nan-Iav), have been localised
45 near the distal and proximal regions of the ciliary dilation, an enlarged region where the
46 axonemal microtubules are farther apart than the rest of the cilium[5–8]. Early studies proposed
47 two primary models for how these channels open: axial extension (stretching)[9–11] or lateral
48 compression (pinching) of the ciliary tip[12]. One prominent axial extension model posits that
49 stretching deforms the ciliary dilation, generating shear forces within the ciliary membrane that
50 open the MET channels[9]. In contrast, the lateral compression model is supported by a similar
51 proposed mechanism in campaniform sensilla, where direct force application on the cap evokes
52 a maximal receptor potential[12]. Alongside the two MET channel opening models—axial
53 extension and lateral compression of the ciliary tip— several other working mechanisms have
54 been proposed based on early ultrastructural and electrophysiological studies[4].

55 A detailed ultrastructure of the scolopidium is key to understanding its function as a
56 mechano-electrical transducer[3,10,13–16]. The first ultrastructural studies of the scolopidium stem
57 from more than 60 years ago[3,16], and only recently has three-dimensional (3D) reconstruction
58 using Focused Ion Beam-Scanning Electron Microscopy (FIB-SEM), been employed to
59 examine a miniaturised chordotonal organ, the Johnston's organ of parasitoid wasp
60 *Megaphragma viggianii*[17]. A high-resolution 3D reconstruction that focuses solely on the
61 scolopidium using FIB-SEM could provide new insights into its ultrastructure, especially how
62 each component interacts.

Complementing these structural insights, efforts to understand the sound-evoked scolopidial motion have yielded valuable, albeit indirect, inferences: Stephen and Bennet-Clark's pioneering stroboscopy of the locust Müller's organ suggested significant phase lags and anti-phasic motion across the organ, potentially inducing strain in auditory neurons and scolopidia[18]. More recently, Optical Coherence Tomography (OCT) based vibrometry of the cricket's crista acustica indicated complex, multi-modal tilting of the ciliary tip, including 3D elliptical motions[19,20]. Although providing valuable insight, these observations lack the spatial resolution to directly resolve scolopidia. This limitation highlights the critical need for direct visualisation of its sound-evoked motion, and measurement of transduction currents during direct mechanical stimulation of a scolopidium.

To address these gaps, we investigated the scolopidia within Müller's organ of adult desert locusts, *Schistocerca gregaria*, a model organism that uniquely enables recordings of transduction channel currents from auditory neurons in an adult animal[8]. We combined FIB-SEM to resolve the 3D ultrastructure of a scolopidium, OCT and high-speed microscopy to examine sound-evoked motion at both the organ and individual scolopidium levels, and direct mechanical stimulation of the scolopale cap, where the ciliary tip is anchored, whilst recording transduction currents. Understanding these fundamental processes in insect auditory transduction is not only key to deciphering insect hearing but offers insights into conserved principles of ciliary mechanosensation across animals.

2. Results

2.1. Three-dimensional (3D) ultrastructure of a scolopidium

The desert locust's tympanic ears are located on its first abdominal segment (Fig. 1a). The locust's hearing organ, Müller's organ, directly attaches to the tympanic membrane at an inward fold of the tympanum called the elevated process (Fig. 1b). Auditory neuron soma locate mostly in the ganglion, while their dendrites extend to distinct regions of the organ, forming three classified groups also distinguished by characteristic frequency ranges[8,21] (Fig. 1c, Extended Data Fig. 1a-c). This study examines scolopidia from Group-III auditory neurons (Fig. 1c, d), which constitute most auditory neurons (~48 out of ~80 neurons) in Müller's organ[22] and are tuned to 2.5-4 kHz[1], the frequency ranges associated with wing-beat noise[23].

To reconstruct a 3D ultrastructure of a scolopidium, we performed Focused Ion Beam-Scanning Electron Microscopy (FIB-SEM) at the interface between the scolopale cells and the attachment cells, where the scolopidia are located (Fig. 2a-b, see Supplementary Video 1) (N = 2, n = 4). In this region, the scolopale cell forms a protrusion that encloses the scolopale sheath with approximately half of the sheath inserting deep into the attachment cell. The scolopale sheath, previously described as composed of 5-7 partially fused, actin-rich concentric rods, is contained within the scolopale cell[3,24]. In early ultrastructural studies, the distal region of the scolopidium was thought to end with the extracellular porous cap[3,9,10,14]; however, our 3D reconstruction reveals a thin layer of fibrous filaments, possibly actin filaments, forming inside the membrane of the attachment cell (Fig. 2c, arrowhead). Upon examining series of longitudinal sections along the length of the scolopidium, this fibrous material covers the distal end of the ciliated dendrite and the cap like a cone-shaped 'lid' (Fig. 2d, arrowheads). Thus, we describe the ensheathed part of a scolopidium as a cartridge composed of the scolopale sheath and a scolopale lid (Fig. 2l).

The scolopale cartridge encloses a tightly sealed receptor-filled scolopale space that contains the ciliated dendrite and the porous cap (Fig. 2b). Our 3D reconstruction reveals that the cap resembles a truncated cone, with a central passage for the cilium that is funnel-shaped and has a distinct narrowing at its entrance (Fig. 2e-f). An early ultrastructural study of Müller's organ reported that the cilium terminates within the cap[3]; however, we find that the cilium instead extends through the central passage and terminates at an electron-dense region at the tip of the cartridge, in the three scolopidia we imaged (Fig. 2g, Extended Data Fig. 1d). Interestingly, one of our datasets shows a break of the cilium near its terminus (Extended Data

Fig. 1e). The cilium's full extension to its insertion at tip of the cartridge is a prominent, previously undescribed feature with clear mechanical implications.

At the distal dendrite, the cilium is anchored through rootlets. Here, numerous basal links connect the dendritic membrane to the base of the scolopale sheath and form an oblique angle of about 50° to the dendrite (Fig. 2h). The basal links show no apparent spacing and are found from the base of the scolopale sheath up to the proximal basal body, where the cilium inserts into the scolopale space. In a cross section orthogonal to the ciliary axis, the basal links appear to radiate towards the dendrite from desmosome-like junctions at the scolopale cell membrane opposing each scolopale rod (Fig. 2i). The basal links and their connections to the base of each scolopale rod have been previously shown[9,10,25], but the oblique nature of the links has not been observed before.

The proximal cilium exhibits a pronounced bending in all our datasets, a feature previously observed in other chordotonal organs[4,11,26]; however, we cannot rule out fixation artifacts due to preparation for FIB-SEM. In contrast, the distal cilium remains straight (Fig. 2b, l). In the ciliary dilation, where the 9x2+0 axonemal microtubules become farther apart, we found 3-4 central fibrils appearing within the restricted length of the dilation but nowhere else (Fig. 2j-k, Extended Data Fig. 1f-g). While these central fibrils have been mentioned by early ultrastructural studies[3,9] and observed in crista acustica of the bush cricket, *Mecopoda elongata*[19], their precise nature remains unclear and requires further investigation.

In summary, our high-resolution 3D ultrastructural analysis has redefined the ensheathed part of the scolopidium as a 'cartridge' composed of the scolopale sheath and scolopale lid (Fig. 2l). This analysis also revealed the full extent of the cilium (Fig. 2g), the oblique nature of the basal links (Fig. 2h), and the central fibrils in the dilation (Fig. 2j-k). This refined anatomical understanding is crucial for interpreting how forces are transmitted within this mechanosensory unit. We, therefore, next examined the sound-evoked motion at the levels of Müller's organ and individual scolopidium to determine how these intricate structures may contribute to mechano-electrical transduction.

2.2. Sound-evoked motion of Müller's organ is tuned differently across its axes

The tympanic membrane vibrates in response to sound pressure changes in the air[27–29]. The sound-evoked vibration is then transferred to Müller's organ and mechanically activates the scolopidia inside[21,27]. The resulting motion of the organ is complex and frequency-selective, arising from both the tonotopic traveling wave across the tympanic membrane and the organ's attachment to mechanically inhomogeneous regions on the tympanum[18,27,29]. Ultimately,

however, only the relative motion within the organ can produce forces that serve as the adequate stimulus for auditory transduction.

To identify the source of this relative motion, we measured the sound-evoked vibrations of Müller's organ along two primary axes (Fig. 3a): (i) antero-posterior (motion normal to the tympanic surface, Fig. 3a-top panel) and (ii) meso-lateral (motion tangential to the tympanic surface, Fig. 3a-bottom panel). The OCT imaging system could generate sectional images across the two planes (Fig. 3b) and resolved most of the organ, apart from the region of Group-I scolopidia above the folded body, possibly due to low reflectivity (Fig. 3b).

We first examined the frequency response of Müller's organ relative to sound stimulation (Fig. 3c-d). The vibration was axis-dependent: along the antero-posterior axis, the amplitudes peaked at 3.75 kHz, 7.58 ± 6.24 dB (N = 4, E = 4), while the meso-lateral axis showed a distinct peak at 2.25 kHz, 13.07 ± 3.62 dB (N = 7, E = 12) (Fig. 3c). There is also relatively high vibration at 1 kHz in both axes, antero-posterior: 9.82 ± 6.65 dB (N = 4, E = 4) and meso-lateral: 8.61 ± 4.33 dB (N = 7, E = 12). The phase responses relative to the stimulation in the two axes also differed. While both axes exhibited a phase lag of approximately ~0.5 cycles, anterior-posterior: -0.47 ± 0.11 cycle (N = 4, E = 4) and meso-lateral: -0.57 ± 0.17 cycle (N = 7, E = 12), the phase response in meso-lateral axis showed a more pronounced ~1-cycle lag at its 2.25 kHz peak, -0.90 ± 0.49 cycle (N = 7, E = 12) (Fig. 3d). Vibration at 1-2 kHz and 3.75 kHz corresponding to known resonance modes of the entire tympanum and the Müller's organ region[27].

To assess the internal strain across the organ, we further computed vector difference of the styliform body (●, Fig 3b) relative to the ganglion (*, Fig 3b), the region where Group-III scolopidia are located. Vector difference revealed two prominent peaks at 3.75 kHz along the antero-posterior axis, 6.81 ± 8.78 dB (N = 4, E = 4), and 2.25 kHz along the meso-lateral axis, 12.18 ± 9.55 dB (N = 7, E = 12). The small vector difference at 1.25 kHz in both axes, antero-posterior: 1.31 ± 9.04 dB (N = 4, E = 4) and meso-lateral 2.67 ± 8.68 dB (N = 7, E = 12), indicates no or very small relative motion in the region of Group-III scolopidia at this frequency (Fig. 3e). Next, we mapped these complex, frequency-dependent vibration patterns onto the locations of Group-III scolopidia.

179 **2.3. Relative motion at the site of Group-III scolopidia**

180 We mapped Group-III scolopidia by labelling their auditory neurons with the neural tracer
181 neurobiotin, delivered via back-filled patch pipettes through the auditory nerves[30]. Since the
182 scolopidia themselves were not consistently labelled, we used their dendrite dilations as reliable
183 proxies (Fig. 1d). The position of each dendrite dilation was manually registered relative to the
184 ganglion and the styliform body (Extended Data Fig. 2a-c). These dilations locate at a known
185 distance, 11.1 ± 3.7 µm (N = 20, n = 46), from the base of the scolopale sheath (Extended Data
186 Fig. 2d). Ensemble normalised positions of the dendrite dilations revealed that Group-III
187 scolopidia are clustered at a relative distance 54 ± 4% (N = 16, E = 16, n = 253) between the
188 ganglion and the styliform body (Fig. 3f).

189 Having established the location of the Group-III scolopidia, we analysed the 2D vibration
190 profiles to determine if this location corresponds to a region of high relative motion (Fig. 3g-
191 h). Indeed, we observed that while motion was largely homogeneous at low (1 kHz) and high
192 (5 kHz) frequencies, a distinct spatial transition emerged at the intermediate frequencies. Along
193 the antero-posterior axis, an abrupt change in both amplitude and phase appeared from 2 kHz
194 upwards, with the largest transition occurring at ~4 kHz (Fig. 3g arrowhead, Extended Data
195 Fig. 2e-f). A similar sharp transition was observed in the meso-lateral axis, though its peak
196 occurred at a lower frequency of ~3 kHz (Fig. 3h, Extended Data Fig. 2g-h). Interestingly, upon
197 examining the vibration profile (Extended Data Fig. 2e, g), the source of vibration appeared to
198 shift with frequency. At lower frequencies (1.25-2 kHz), the ganglion side of the organ vibrated
199 more strongly (~2.5-4 dB) than the styliform body, while at higher frequencies the vibration
200 was larger at the styliform body and the tympanum (Extended Data Fig. 2e-h). Crucially, upon
201 superimposing the normalised position of Group-III scolopidia on the frequency response for
202 both axes, the onset of this abrupt transition in amplitude and phase co-localizes precisely with
203 the average position of the Group-III scolopidia (Fig. 3i, j and Extended Data Fig. 2). To
204 understand how this complex relative motion activates the scolopidium, we visualized the
205 sound-evoked motion of individual scolopidium with high-speed light microscopy.

206

207 **2.4. Elliptical motion and stretching of a scolopidium along the ciliary axis**

208 To examine sound-evoked motion at the single-scolopidium level, we captured its high-
209 speed motion during sound stimulation (Supplementary Video 2) and achieved an average
210 acquisition rate of 8,602 ± 289 frames per second (N = 12, n = 48). Upon initial image analysis,
211 we found two prominent features (Fig. 4a-b): (i) shearing and stretch motion of the scolopidium
212 (Fig. 4a, t = 0.12 and 0.24 ms) then followed by (ii) pulling motion of the scolopale sheath

along the ciliary axis (Fig. 4a, t = 0.36 ms). The shearing and stretch motion were most clearly visible at the cap region, where the membrane of the attachment cell deforms. To quantify these complex scolopidium motion, we tracked the positions of the scolopale base and the extracellular cap, where the outlines of both landmarks were clearly visible (Fig. 4a)).

First, we analysed the raw amplitude of the scolopale base and the cap. Upon sound stimulation, the entire scolopidium undergoes elliptical motion (Fig. 4c). Notably, the motion of the scolopale base was generally more circular, while that of the cap was more elliptical, particularly between 1.5-3 kHz. At 1 kHz; however, the scolopidium shows a strong elliptical motion oblique to the ciliary axis. When stimulated at 3 kHz, the elliptical motion of the cap aligned with the ciliary axis and was most pronounced.

To investigate the principal axis of the sound-evoked motion, we decomposed the motion of both the cap and the scolopale base into components along the ciliary axis, d_x, (Fig. 4d) and orthogonal to it, d_y, (Fig. 4e). For both landmarks, motion along the ciliary axis was strongest, showing a prominent peak at 3 kHz, base d_x: 66 ± 55 nm (N = 6, n = 24) and cap d_y: 197 ± 64 nm (N = 6, n = 24), (Fig. 4d, Extended Data Fig. 3a, c). In contrast, orthogonal motion was minimal, exhibiting only a shallow peak at the same frequency, base d_x: 47 ± 26 nm (N = 6, n = 24) and cap d_y: 70 ± 44 nm (N = 6, n = 24), (Fig. 4e, Extended Data Fig. 3b, d). Consequently, the ratio of axial-to-orthogonal motion, d_x/d_y, is consistent with elliptical motion shown in Fig. 4c, where cap d_x/d_y peaked sharply at 3 kHz, base d_x/d_y: 1.29 ± 0.66 (N = 6, n = 24) and cap d_x/d_y: 2.72 ± 1.00 (N = 6, n = 24), confirming that axial motion is the dominant component of the frequency response (Fig. 4f).

Since the adequate stimulus for MET is expected to arise from relative motion within the scolopidium, we next computed (i) the relative distance between the cap and the scolopale base, Δd, and (ii) shear motion at the cap region quantified by tracking the upper and lower borders of the attachment cell upon sound stimulation. Indeed, the relative motion was also strongest and sharply peaked at 3 kHz, Δd: 74 ± 48 nm (N = 6, n = 24) (Fig. 4g-h). The shear motion of the cap region; however, produced a distinct but broad peak at 3 kHz, 215 ± 200 nm (N = 6, n = 22) (Fig. 4i).

2.5. Direct pulling of the scolopidium cap evokes maximal transduction current

High-speed light microscopy revealed complex sound-evoked motion of the scolopidium mainly, but not solely, along the ciliary axis (Fig. 4). To identify the principal axis through which the scolopidium is stimulated, we directly and mechanically stimulated the scolopidium

246 cap with a stimulating pipette while measuring transduction currents via whole-cell patch-
247 clamp recordings of the corresponding Group-III auditory neuron somata (Fig. 5a;
248 Supplementary Video 3). We delivered a series of step displacements in two directions: a 'pull-
249 push' motion along the ciliary axis (Fig. 5b) and an 'up-down' motion orthogonal to it (Fig. 5c).
250 Here, we showed that stimuli in pull, push, upward and downward directions evoked sharp,
251 transient inward currents at the onset of the step (Fig. 5d-e). The most sensitive responses were
252 to pull and push stimulations at 1 nm (Fig. 5d), whereas upward and downward stimulations
253 produced clearly noticeable transduction currents from 5 nm and above (Fig. 5e). The signal-
254 to-noise ratio in single trials was low due to spontaneous discrete depolarisations found in
255 chordotonal organs[6,8,31]. Upon averaging the responses over the total number of locusts, pull-
256 push: N = 18, n = 18 and up-down: N = 11, n = 11, the ensemble average transduction current
257 revealed a graded, non-linear relationship between stimulus and current (Fig. 5f-g).
258 Next, we quantified transduction currents in response to pull-push step stimuli averaged
259 across all recordings. There was a general increase in the magnitude of the transduction current
260 with increased step displacement (Fig. 5h, i). Discrete depolarisations contributed to a large
261 standard deviation of step-evoked transduction currents (Fig. 5d, e). There were distinct bi-
262 phasic and logarithmic phases in the current-displacement (I-X) relationship from 1-10 nm and
263 50-2000 nm in both pull-push (Fig. 5j, k) and up-down (Fig. 5l, m) displacements. The largest
264 transduction currents were produced by pull along the ciliary axis. We quantified the difference
265 at 2,000 nm displacement from the resting position between pull, 26.22 ± 10.99 pA (N = 18, n
266 = 18), and push, 10.96 ± 8.59 pA (N = 18, n = 18) (Tukey's procedure, p = 3.1e-05, t = -9.58).
267 Next, we found that the transduction current was larger for $pull_{return}$, 18.68 ± 8.43 pA (N = 18,
268 n = 18) compared to $push_{return}$ 6.99 ± 9.75 pA (N = 18, n = 18) (Tukey's procedure, p = 0.003,
269 t = -4.72). Additionally, the transduction current evoked by pull from the resting position was
270 larger than displacement upward, 12.17 ± 5.37 pA (N = 11, n = 11) (Tukey's procedure, p =
271 1.75e-03, t = -3.83) or downward 7.28 ± 9.76 pA (N = 11, n = 11) (Tukey's procedure, p =
272 5.10e-06, t = -4.53). There was no difference between $pull_{return}$ and $up_{preturn}$ (Tukey's procedure,
273 p = 0.69, t = -1.91), and between $pull_{return}$ and $down_{return}$ (Tukey's procedure, p = 0.55, t = -2.24).

274

275 **3. Discussion**

276 The scolopidium is the basic sensory unit of mechano-electrical transduction (MET) in
277 insects[3,9,11,12,14,25]. Addressing the fundamental question of how the scolopidium operates, we
278 demonstrate here that axial stretch along the cilium is the adequate stimulus for mechano-
279 electrical transduction. This conclusion is based on two key findings. First, high-speed imaging
280 revealed that elliptical sound-evoked scolopidium motion is dominated by stretch along the
281 ciliary axis (Fig. 4). Second, pull of the scolopidium along the ciliary axis evoked the maximal
282 MET current (Fig. 5).

283 Axial stretch is assumed to be the adequate stimulus in other chordotonal organs, based on
284 either ultrastructural analysis or electrophysiological recordings, without direct observation of
285 the underlying mechanics[9,11,32]. These early studies, performed before the molecular identity
286 and precise location of MET channel candidates like NompC and Nan-Iav were known, led to
287 at least ten proposed mechanisms[4,33]. For example, deformation of the ciliary dilation[9,11,32],
288 bending of the cilium[11,32] or scolopale sheath[24,34], and contraction of the ciliary rootlet [34]. Yet
289 another hypothesis proposed that the cap that encloses the cilium could narrow during axial
290 stretch and exert a compressive force to the ciliary membrane[12]. Our finding provides the first
291 direct evidence that axial stretch is the adequate stimulus of this highly conserved
292 mechanoreceptor found in all insects[35].

293 How does stretch of the scolopidium lead to confirmational change of MET channels within
294 the cilium? Here, we propose three competing hypotheses: (i) In the *'stretch model'*, axial
295 tension is transmitted along the ciliary membrane, stretches the lipid bilayer and opens MET
296 channels. (ii) In the *'stretch-compression model'*, axial stretch narrows the central passage of
297 the cap and thus compressing the ciliary tip i.e. when a compressive material with a hollow
298 tube is deformed along its axis, the tube narrows (like a 'Chinese finger trap'). (iii) In the
299 *'stretch-deformation model'* the larger ciliary dilation is pulled against the narrow central
300 passage of the cap (Fig. 2e, f). In short, the MET channels would be opened through membrane
301 tension in the stretch model, but by compressive forces directly onto the membrane in the
302 stretch-compression and stretch-deformation models.

303 While a complete gating model for insect MET remains elusive[36], key molecular insights
304 have been provided by the cryo-EM structure of the putative channel NompC[37], as well as by
305 Molecular Dynamics (MD) simulations[38,39], and electrophysiological recordings[38,40,41].
306 Specific structures within NompC, such as its Ankyrin Repeat (AR)[41,42] and Linker Helix

307 (LH)[40] domains, have been proposed to form a "gating spring"—a compliant element that
308 transmits mechanical force into the channel's conformational opening[40,43].
309 Currently, there is no direct evidence to support a 'direct-stretch model.' However,
310 compelling evidence does support the stretch-compression and the stretch-deformation models.
311 In particular, NompC expressed in Drosophila S2 transfected cells are more sensitive to
312 membrane compression than aspiration[38]. The other MET channel candidate Nan-Iav is not
313 mechanosensitive when expressed in HEK293T cells[7]. The properties of both of these TRP
314 channels may operate differently in the cilium compared to heterologous cell lines. If
315 Nanchung-Inactive was mechanosensitive in the cilium then stretch, not compression, would
316 be the only feasible mechanism for MET channel opening.
317 Our OCT-based vibrometry reveals that axial stretch of the scolopidium arises from
318 complex 3D motion of Müller's organ[18], a feature that maybe shared by other chordotonal
319 organs[19,44,45]. We demonstrate that there was an abrupt transition in both phase and amplitude
320 localised at the site of Group-III scolopidia, which would generate relative motion across the
321 ciliary axis (Fig. 3 g, h). While motion along the antero-posterior axis is largely dominated by
322 the tympanum's movement at 3.5-4 kHz[27], strong vibrations along the meso-lateral axis at
323 lower frequencies, 2.25-3 kHz (Fig. 3c, e), may contribute to broad frequency sensitivity of the
324 sound-evoked transduction current[1] .
325 Finally, our high-resolution 3D ultrastructure provides the anatomical framework for how
326 the scolopidium operates (Fig. 2). The presence of scolopale 'lid' and the full extent of the
327 cilium to its insertion at the scolopale cartridge tip indicate a firm, direct coupling between the
328 attachment cell and the cilium, essential for transmitting tensioning force. Furthermore, the
329 distinct narrowing at the entrance to the central passage may serve to compress the cilium
330 during axial stretch (Fig. 2e, f). The numerous oblique basal links may not be directly involved
331 in transduction but likely provide mechanical stability to the distal dendrite and ciliary rootlet
332 (Fig. 2h, i). The nature of the central fibrils within the ciliary dilation (Fig. 2j, k) remains
333 unknown but are also in bush cricket and mosquito auditory neuron cilia[19,46].
334 In conclusion, our study provides a comprehensive, multi-scale analysis of MET in the
335 insect auditory chordotonal neuron, using excised preparations of locust ears. We have shown
336 that complex 3D motion of Müller's organ produces localised relative motion precisely where
337 the auditory scolopidia are situated. This relative motion within the organ then drives an axial
338 stretch of the scolopidium, which in turn evokes the mechano-electrical transduction current.
339 As the scolopidial structure is ubiquitous across insect classes, the fundamental mechanism of
340 MET activation proposed here is likely to be highly conserved.

4. Acknowledgments

We thank Daisy Ogle and Alix Blockley for providing z-stack images of Dylight-488 conjugated streptavidin neurobiotin labelled auditory neurons, which allowed us to map the positions of Group-III scolopidia. We are grateful to Celia Hansen and Ramesh Patel for maintaining the locust facility. Focused Ion Beam Scanning Electron Microscopy (FIB-SEM) was performed by Claire Boulogne at the Electron Microscopy facility of Imagerie-Gif, Institute for Integrative Biology of the Cell (I2BC). Sample preparation for electron microscopy was assisted by Natalie Allcock and Josh Whittingham. An X-ray micro-CT scan was performed with the help of Gareth Douglas. We also thank Kanpong Boonthaworn for valuable feedback on the manuscript. This project was funded by a Long-term Human Frontier Science Program (HFSP) Fellowship (LT0002/2023-L) and a France Bioimaging Access Grant (Access-4942) awarded to A.C., as well as a University Research Fellowship from the Royal Society awarded to B.W. (URF\R1\180022 & URF\R\231029).

5. Author contributions

A.C. and B.W. designed and planned the experiments. A.C. performed Focus-Ion Beam Scanning Electron Microscopy (FIB-SEM), annotation, and three-dimensional reconstruction of the data from FIB-SEM slices. M.V.H. and M.W. performed the initial phase of Optical Coherence Tomography (OCT) experiments, A.C. and B.W. finalised the data collection and analysis. B.W. performed whole-cell patch clamp recordings. A.C. and B.W. analysed the experimental data and prepared the initial version of the manuscript. M.N. and M.V.H. commented on it, and together with A.C. and B.W., finalised the submitted version of the manuscript.

FIGURE LEGENDS

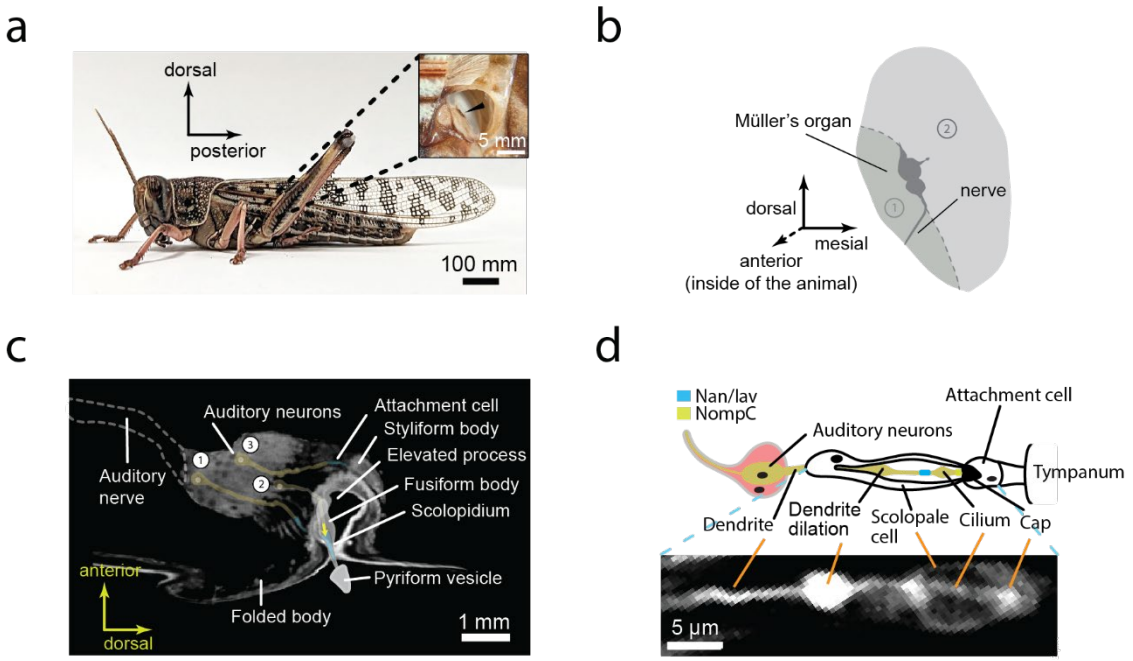

FIGURE 1. The locust's ear, Müller's organ, and the scolodium. (a) Locust's ears are located on the first abdominal segment, hidden behind the wings. Each ear consists of a tympanic membrane with a hearing organ, Müller's organ, directly attached. The surface of the tympanic membrane aligns orthogonally to the antero-posterior axis of the locust body at a slight oblique angle. External view of the tympanic membrane (inset) shows a dark ridge (arrowhead) where Müller's organ is located. The anatomical references used in this manuscript are defined based on the axes of the locust's body unless stated otherwise. **(b)** Illustration of the right ear viewed from inside the body shows Müller's organ located between the 'thick' (1) and 'thin' (2) regions of the tympanic membrane. The auditory nerve projects ventrally toward the ventral nerve cord. **(c)** Schematic of Müller's organ superimposed on an X-ray micro-CT scan slice shows three groups of auditory neurons. These neurons (yellow) extend their dendrites to distinct regions where the distal ciliated end of the dendrites insert into the attachment cells (blue). The auditory neurons of Müller's organ are classified based on their maximal frequency sensitivity. Group-I neurons respond to frequencies between 0.5 and 1.5 as well as 3.5 kHz (~20 cells). Group-II neurons are sensitive to higher frequencies of 10–25 kHz (~13 cells), while most auditory neurons, belong to Group-III and respond to mid-range frequencies of 2.5–4 kHz (~46 cells). The yellow arrow marks a typical location of a scolopidium at the insertion of the scolopale cell into the attachment cells. **(d)** Schematic of a scolopidium indicating locations of the mechano-electrical transduction (MET) channel candidates, NompC (blue) and Nanchung-Inactive (green), near the proximal and distal ends of the ciliary dilation (top). Fluorescent micrograph of the corresponding region of the dendrite and the scolopidium. The auditory neuron is filled with Dylight-488 conjugated streptavidin-neurobiotin (bottom).

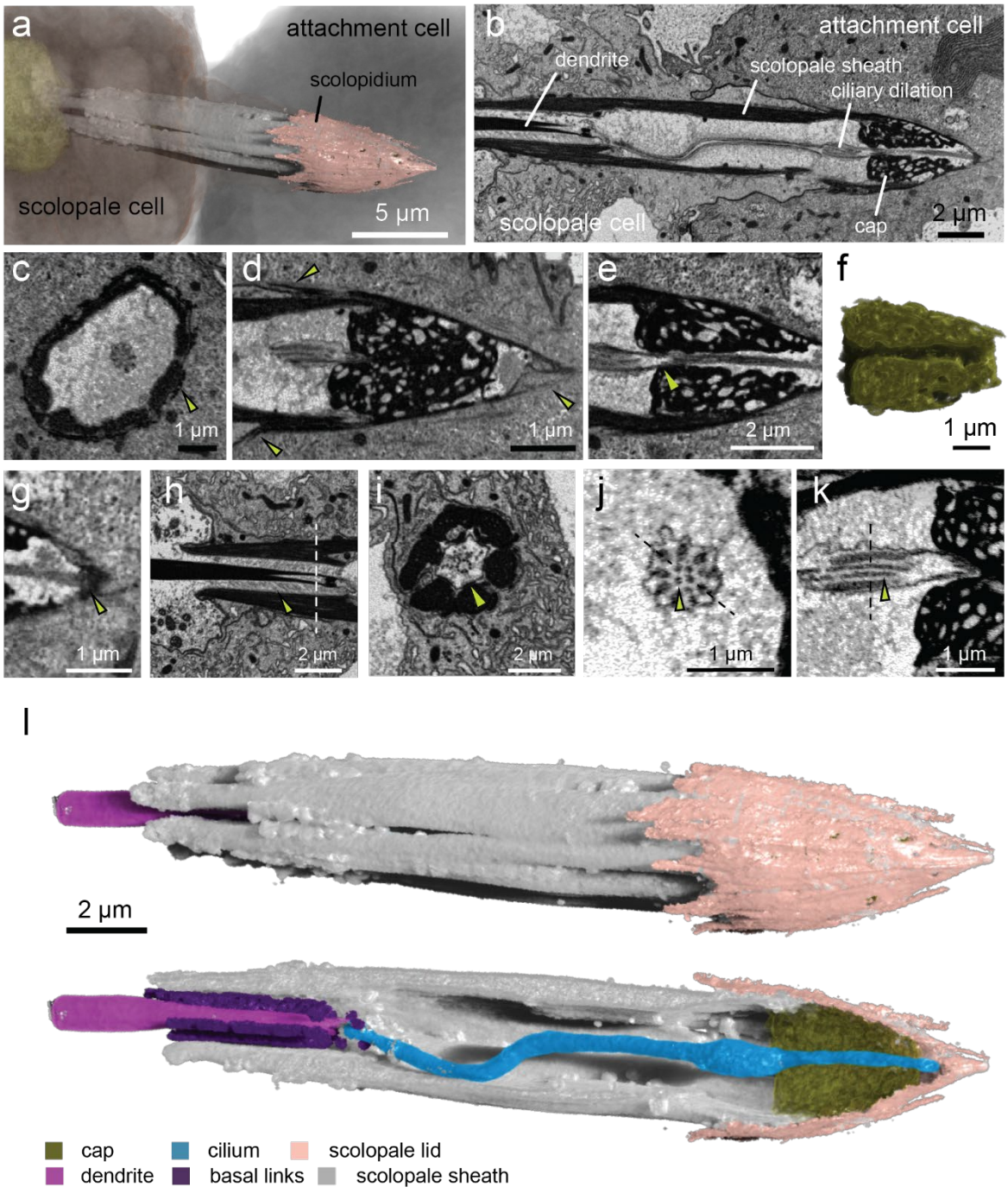

FIGURE 2. Three-dimensional (3D) ultrastructure of a scolopidium. (a) 3D reconstruction at the interface between a scolopale cell and an attachment cell using Focused Ion Beam-Scanning Electron Microscopy (FIB-SEM). **(b)** Longitudinal FIB-SEM slice reveals the dendrite and its ciliated distal end enclosed within the scolopidium sheath; the cilium dilates near its insertion into the porous cap before it terminates in an electron-dense region at the border of the attachment cell. **(c)** Cross section at ciliary dilation shows fibrous filaments inside the membrane of the attachment cell (arrowhead). **(d)** Longitudinal section at the distal region of the scolopale sheath reveals that the fibrous filaments (arrowheads) observed in (c) form a cone-shaped lid covering the cap and the distal region of the ciliated dendrite. **(e)** Longitudinal section at the plane of the cilium shows the narrowing of the central passage, where the cilium enters (arrowhead). **(f)** 3D reconstruction of the cap material reveals a funnel-shaped central passage. **(g)** Termination of the cilium at the extreme end of the scolopale cartridge. **(h)** Longitudinal section at the scolopidium base reveals numerous oblique basal links between scolopale rods and the dendrite. **(i)** Cross section along the dashed line in (h) shows the basal links radiating from desmosome-like junctions. **(j)** Cross section at the ciliary dilation reveals four central fibrils (arrowheads) inside the 9-doublets axonemal structure. **(k)** Longitudinal section along the dashed line in (j) reveals two of the central fibrils along the length of the ciliary dilation. **(l)** 3D model of a complete scolopidium.

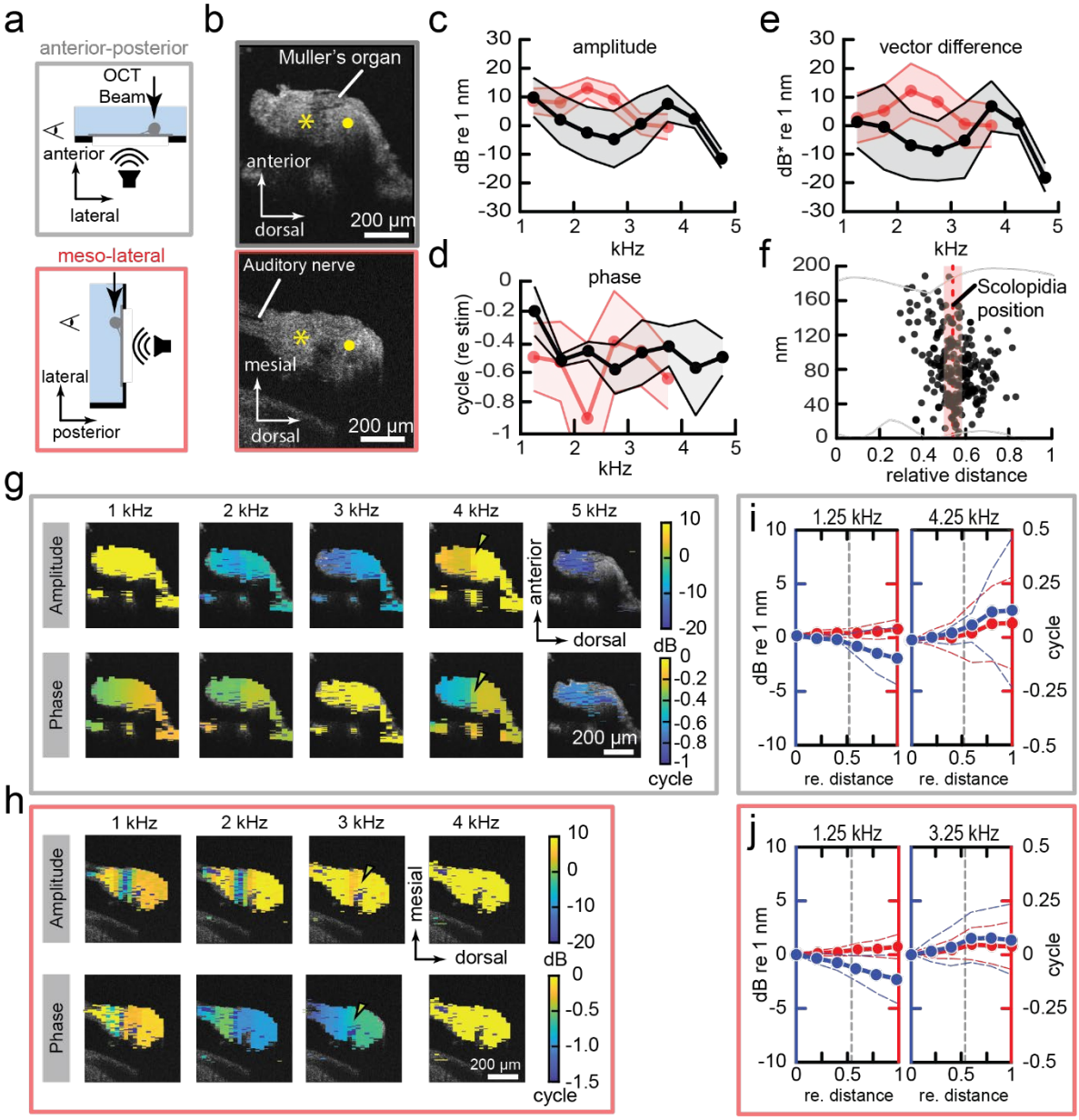

FIGURE 3. Sound-evoked motion of Müller's organ. (a) Vibrometry measurements were performed using Optical Coherence Tomography (OCT) along the antero-posterior (top) or meso-lateral (bottom) axes of Müller's organ upon 90 dB SPL sound stimulation, with the external side of the tympanic membrane facing the loudspeaker. **(b)** OCT sections along the two planes were reconstructed from OCT depth profiles. The symbols * and ● indicate the maximal widths of Müller's organ at the ganglion and the styliform body, the two important landmarks used in our analysis. **(c)** Ensemble amplitude and **(d)** phase responses to stimulated frequencies along the antero-posterior (black, N = 4, E = 4) and meso-lateral (red, N = 7, E = 12) axes. **(e)** Vector difference as a function of stimulated frequency, computed by comparing vibration at the position ● relative to *, as shown in (b), along the antero-posterior (N = 4, E = 4) and meso-lateral (N = 7, E = 12) axes. The responses in (c), (d), and (e) are plotted as a function of bin centres from 1.25 to 4.75 kHz with a bin width of 0.5 kHz. **(f)** Normalised positions of Group-III scolopidia between the ganglion and the styliform body (N = 16, E = 16, n = 235). **(g-h)** Vibration maps as a function of stimulated frequency along (g) the antero-posterior and (h) meso-lateral axes. **(i-j)** Comparison between relative amplitude (blue) and phase (red) responses from the position * to ● along (i) the antero-posterior (N = 4, E = 4) and (j) meso-lateral (N = 7, E = 12) axes. The relative amplitudes are selected from 1.25 kHz (minimal relative amplitude) and at the frequencies where the relative amplitude is largest in each axis, 4.25 kHz and 3.25 kHz, respectively. The relative distance is normalised with * as 0 and ● as 1, as shown in (b). The grey dashed line represents the average Group-III scolopidia position obtained from (f). All vibration amplitudes are shown in dB relative to a 1-nm reference vibration. For additional data, see Extended Data Fig. 2 and Source Data Fig. 3.

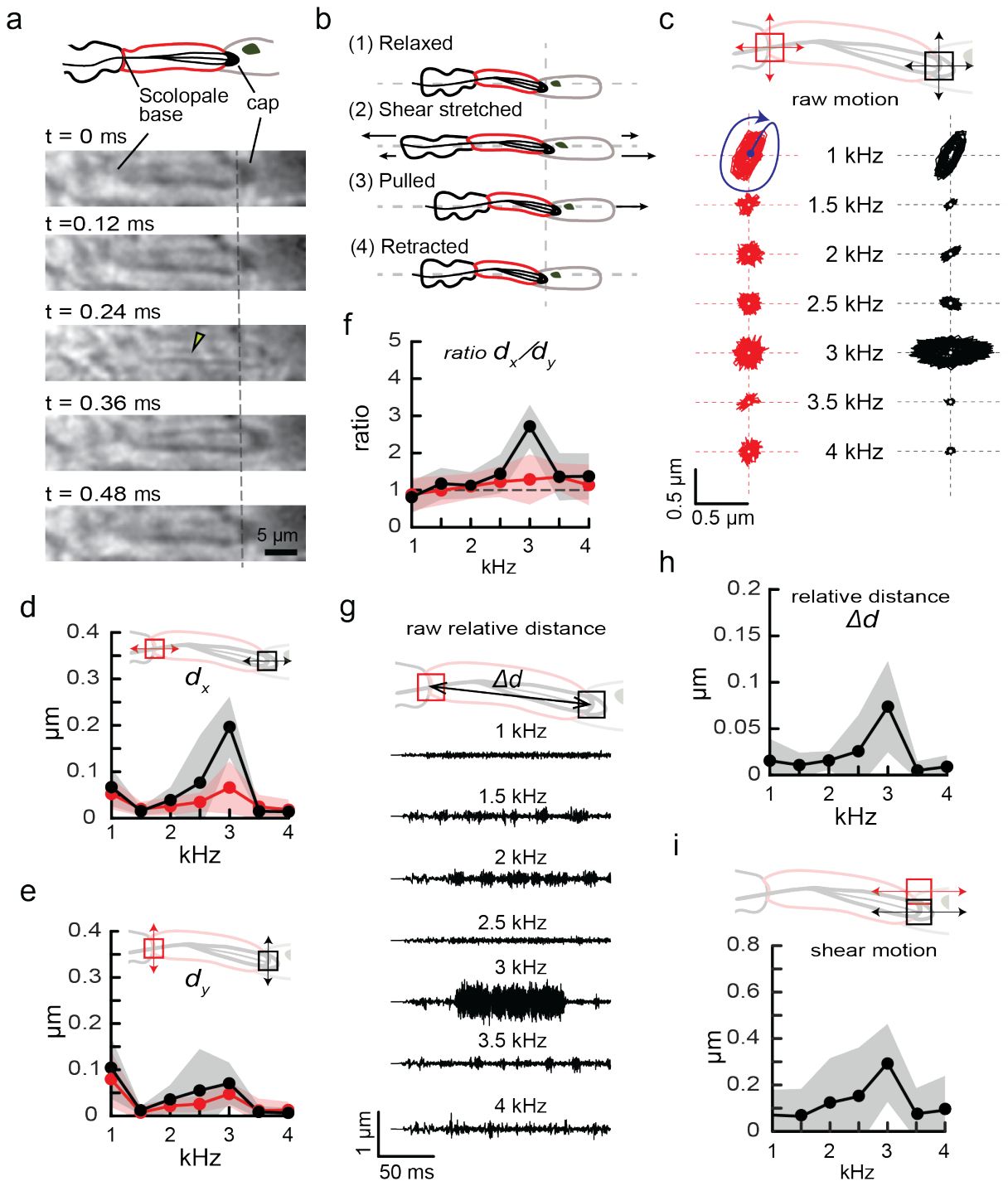

FIGURE 4. Sound-evoked motion of the scolopidium. (a) Schematic of a scolopidium showing the scolopale base and the cap that are clearly visible in light microscopy. (top). Montage over a period of one cycle of sound-evoked motion of a Group-III scolopidium stimulated with 3 kHz pure tone at 90 dB SPL (bottom). The arrowhead indicates the cilium appearing at t = 0.24 ms, when the cilium is brought into focus. **(b)** Summary of the sound-evoked motion of the scolopidium. **(c)** Motion of the scolopale base (red) and cap (black) regions along (d_x) and orthogonal (d_y) to the ciliary axis. **(d)** Root-mean-square (RMS) amplitude of the scolopale base (red, N = 6, n = 22) and the cap (black, N = 6, n = 22) regions along the ciliary axis (d_x). **(e)** RMS amplitude of the scolopale base (red, N = 6, n = 22) and the cap (black, N = 6, n = 22) regions along the orthogonal axis (d_y). **(f)** Ratio of the axial-orthogonal motion (d_x/d_y) of the scolopale base (red, N = 6, n = 22) and the cap (black, N = 6, n = 22). **(g)** Example of distance (Δd) between the scolopale base and the cap region as a function of time over each stimulated frequency. **(h)** Relative distance between the scolopale base and the cap (N = 6, n = 24). **(i)** Shear motion along the ciliary axis at the cap region (N = 6, n = 22. For additional data, see Extended Data Fig. 3 and Source Data Fig. 4.

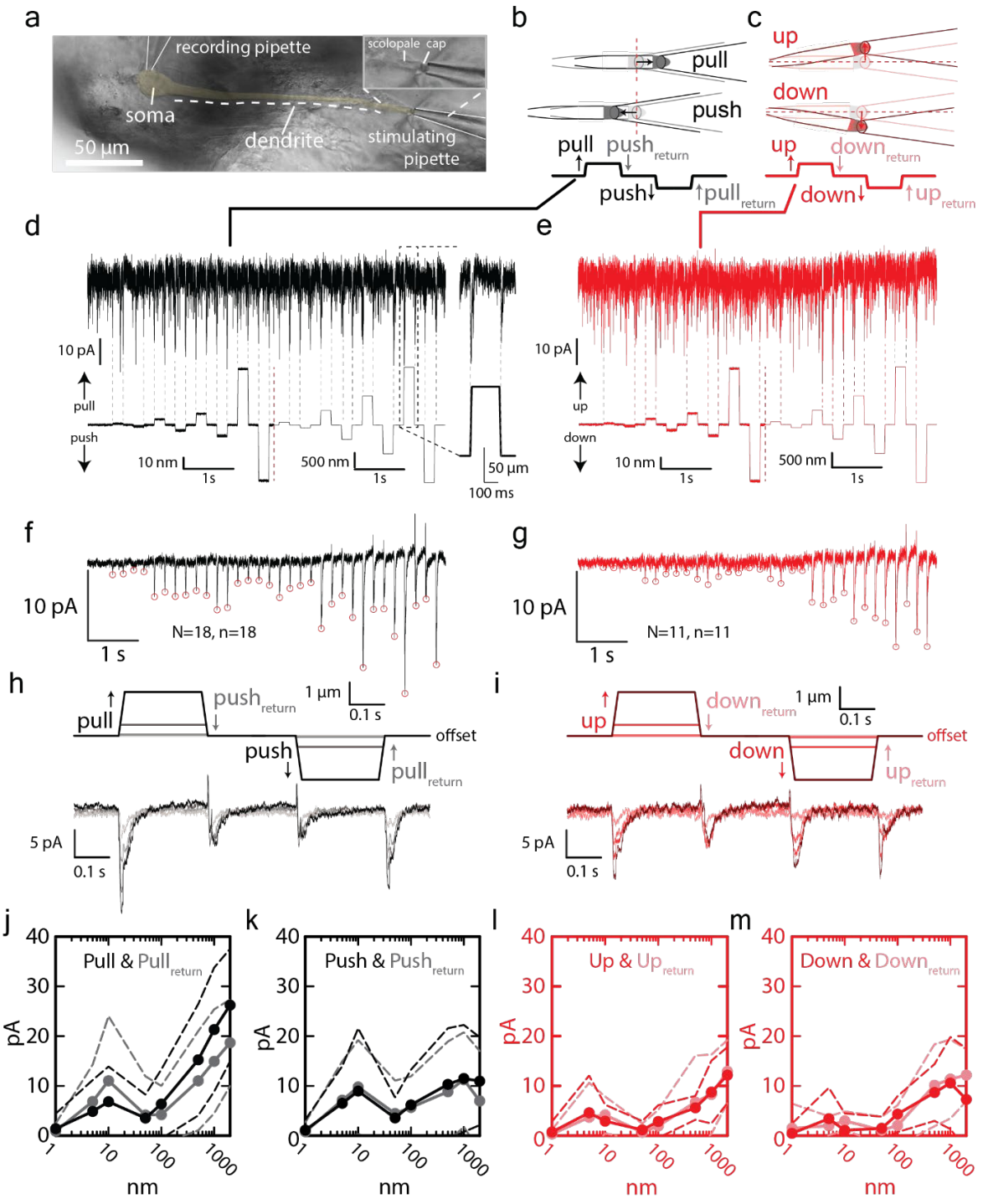

FIGURE 5. Transduction current upon step displacements of a scolopidium cap. (a) Focal-stacked light microscopy image from ~10 µm apart showing the auditory neuron (yellow), a patch recording pipette and an stimulating pipette. **(b-c)** Schematics of step-displacement protocols for (b) pull-push (N = 18, n = 18) and (c) up-down displacements (N = 11, n = 11). **(d-e)** Transduction currents (top trace) in response to (d) pull-push (N = 18, n = 18) and (e) up-down (N = 11, n = 11) displacements (bottom trace). Step-displacement traces below and over 100 nm in (d-e) are shown in different scales. **(f-g)** Ensemble average transduction currents in response to (f) pull-push (N = 18, n = 18) and (g) up-down (N = 11, n = 11) step displacements. **(h-i)** Examples of the transduction currents in response to (h) pull-push and (i) up-down step displacement of magnitudes 2, 50, 500, and 2000 nm. **(j-m)** Ensemble average transduction current as a logarithmic function of the step-displacement (I-log(X) curve) for (j) pull (N = 18, n = 18), (k) push (N = 18, n = 18), (l) upward (N = 11, n = 11), and (m) downward (N = 11, n = 11) displacements with their return to the offset counterparts. For additional data, see Source Data Fig. 3.

EXTENDED DATA FIGURES

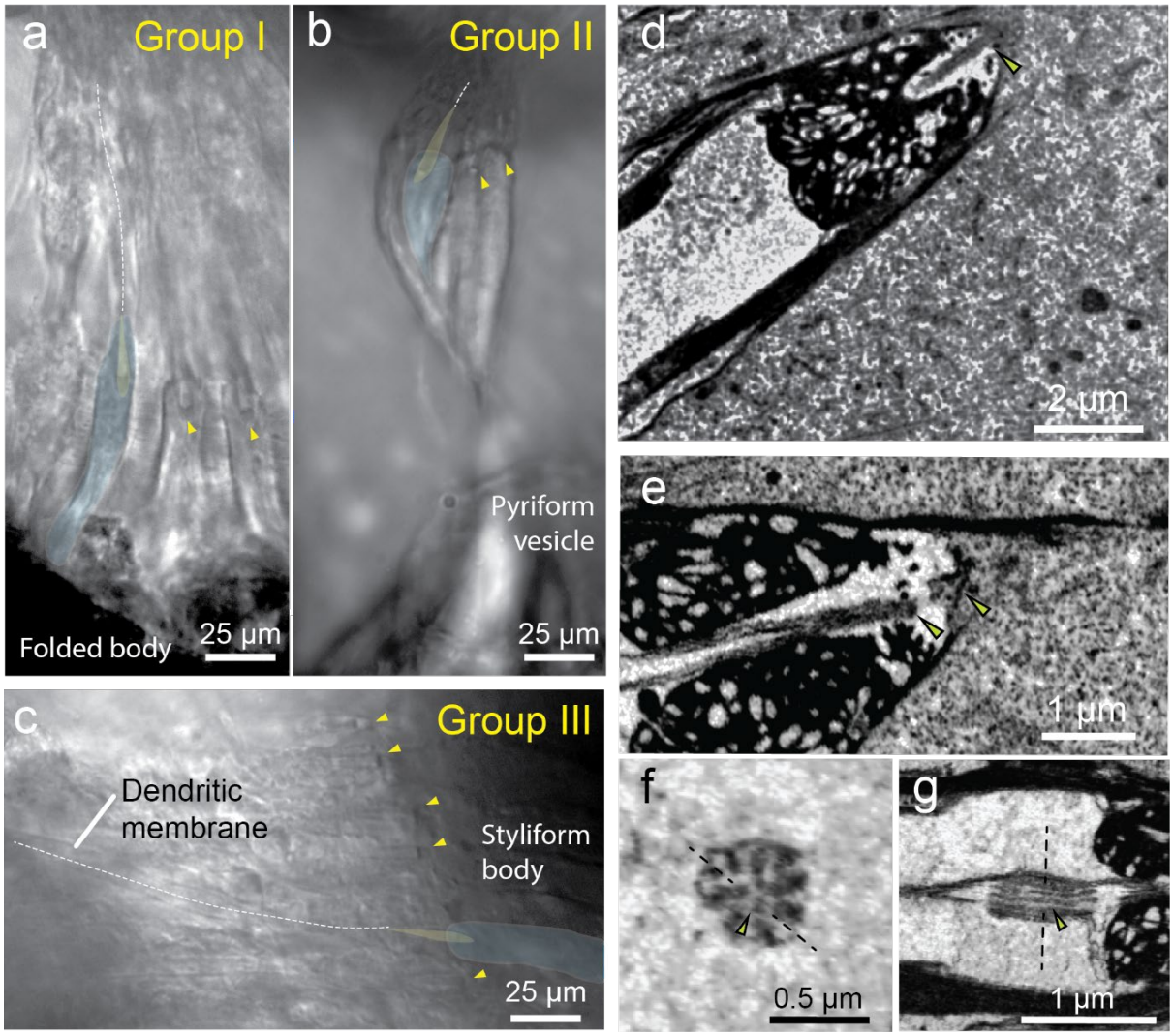

EXTENDED DATA FIGURE 1. Anatomy of the scolopidia. (a-c) Locations of the three groups of scolopidia in Müller's organ: Group-I scolopidia, located near the folded body; Group-II, located within the fusiform body, forming a 'bridge' to the pyriform vesicle at the surface of the tympanic membrane; and Group-III, located on the styliform body. Overlay indicates examples of scolopale sheaths (opaque yellow) and the corresponding attachment cells (blue). Dashed lines outline positions of the dendrites along their lengths, and yellow arrowheads mark the other visible scolopidia. **(d)** Oblique section of the distal region of a scolopidium reveals the full extent of the cilium. **(e)** Example of a potential sample preparation artifact showing the apparent detachment of a cilium from its terminal region. **(f)** Longitudinal section through the ciliary dilation, revealing three central fibrils (arrowhead). **(g)** Longitudinal section along the dashed line in (f), reveals two of the central fibrils (arrowhead) extending along the entire length of the dilation.

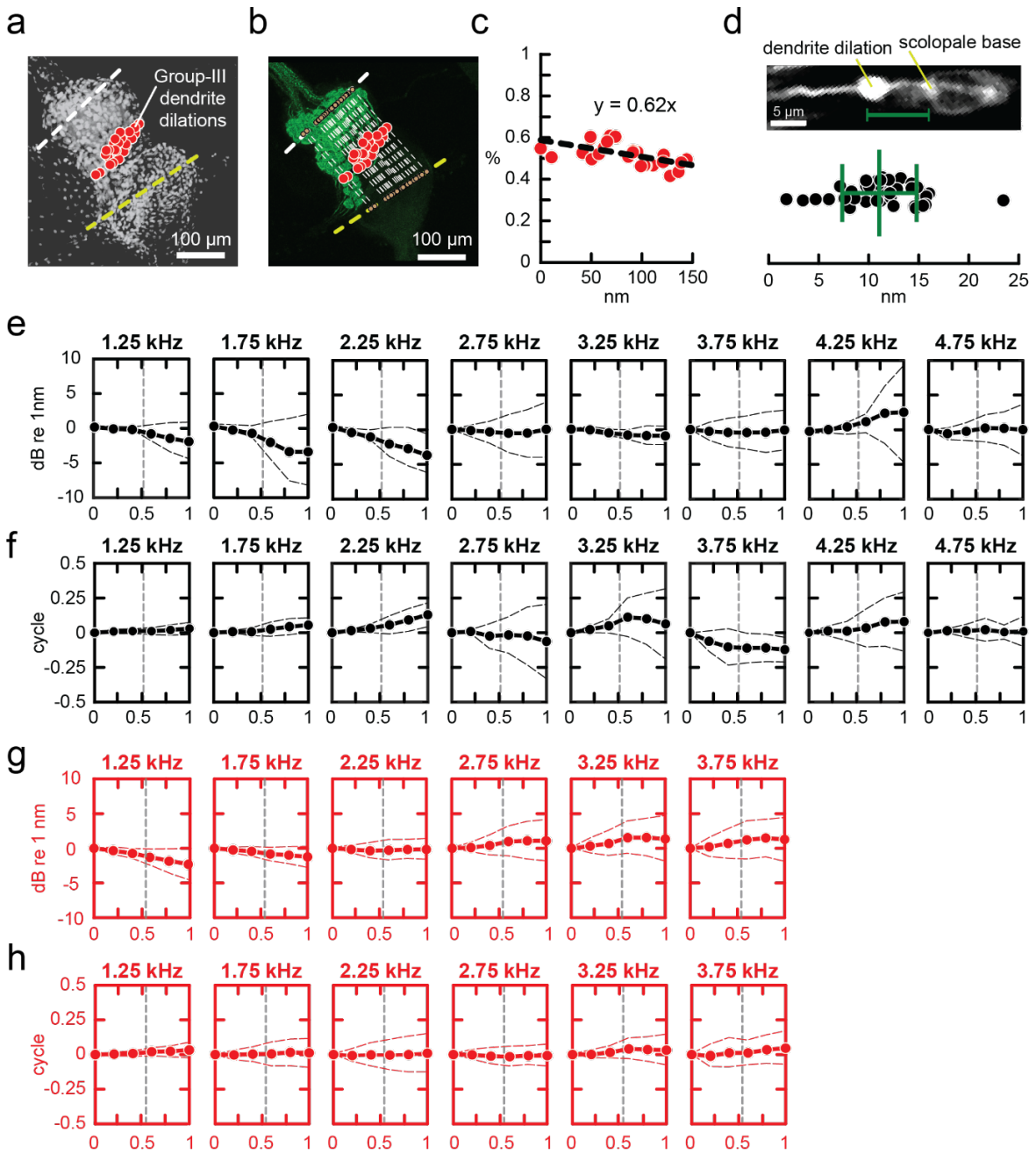

EXTENDED DATA FIGURE 2. Locations of Group-III scolopidia and frequency response of Müller's organ. (a) Maximal intensity projection of a Müller's organ labelled with DAPI superimposed with manual registration of dendrite dilations (red circles). Anatomical landmarks are indicated at the maximal width of the ganglion (white dashed line) and the styliform body (yellow dashed line). **(b)** Maximal intensity projection of auditory neurons labelled with DyLight™ 488-conjugated streptavidin neurobiotin superimposed with manual registration of dendrite dilation (red circles) and schematic illustrating the computation of the relative distance of each dendrite dilation between the ganglion (white dashed line) and the styliform body (yellow dashed line). **(c)** Normalised positions of dendrite dilation from an example of one Müller's organ. The normalised positions of the dendrite dilations are plotted as a function of distance across the ganglion's width (white dashed line axis). A linear fit (black dashed line) determines the representative normalised position at 62% between the ganglion and the styliform body. **(d)** Distances between dendrite dilations and the base of their corresponding scolopale sheath (N = 19, n = 46). **(e, f)** Amplitude (e) and phase (f) response of Müller's organ along the antero-posterior axis (N = 4, E = 4), plotted as a function of relative distance between the ganglion and styliform body. **(g, h)** Amplitude (g) and phase (h) response of Müller's organ along the meso-lateral axis (N = 7, E = 12) plotted as a function of relative distance between the ganglion and styliform body. The vertical dashed lines in (e-h) indicate the normalized position of the Group-III scolopidia. All vibration amplitudes are shown in dB relative to a 1-nm reference vibration. For additional data, see Source Data Extended Fig. 2.

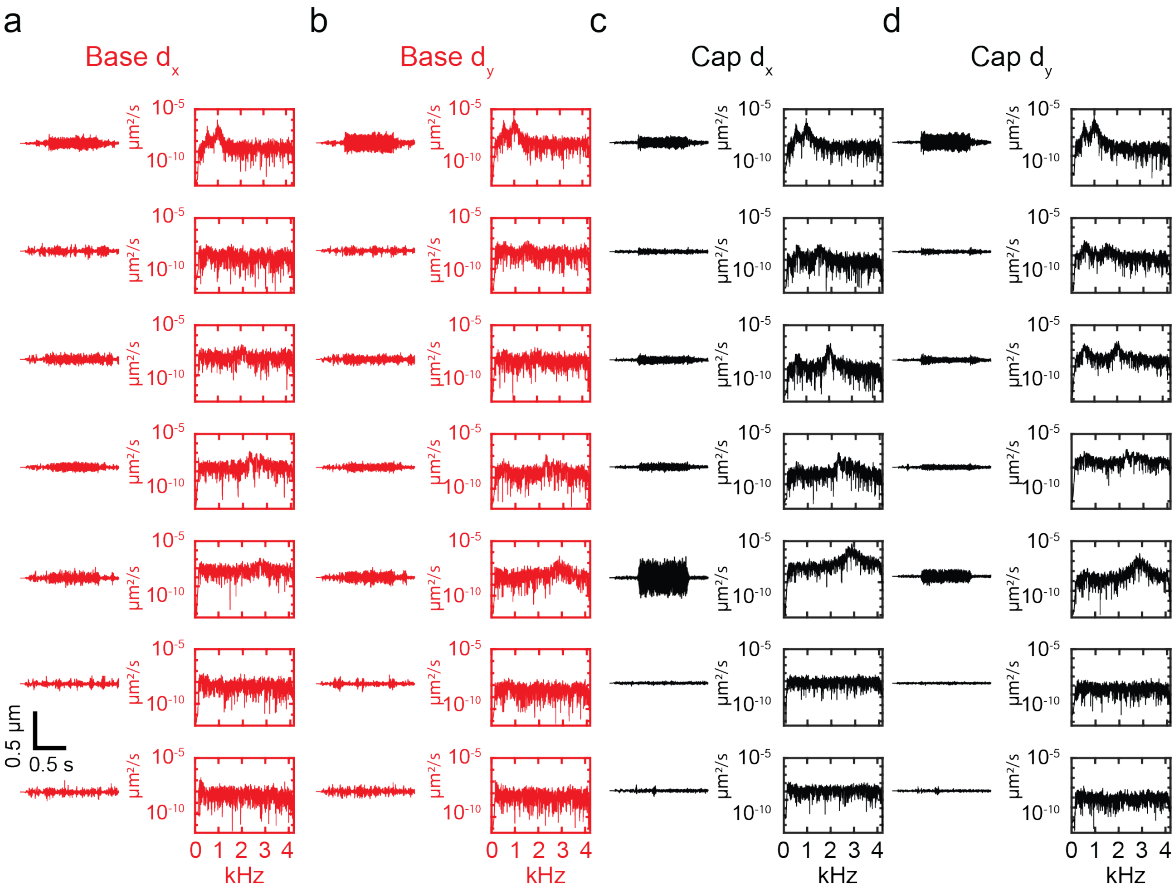

EXTENDED DATA FIGURE 3. Example recordings of sound-evoked motion of a scolopidium. Raw amplitude traces (left traces) and their corresponding Fourier transforms (right traces) for the scolopale base and cap along (d_x) and orthogonal (d_y) to the ciliary axis at each stimulated frequency. **(a, b)** Motion of the scolopale base (a) along and (b) orthogonal to the ciliary axis. **(c, d)** Motion of the cap (c) along and (d) orthogonal to the ciliary axis. Pure-tone sound stimulation at 90 dB SPL. Additional data is available in the public depository, see Data availability.

485 **METHODS**

486 **Animals and sample preparation**

487 Desert locusts, *Schistocerca gregaria*, were reared under crowded conditions with a 12:12-
488 hour light/dark cycle and the ambient temperature at 36 °C (light) and 25 °C (dark). They were
489 fed fresh wheat and bran. All experiments used adult male and female locusts 10-20 days after
490 their final moult.

491 We used an excised locust ear preparation for all experiments, following a previously
492 described dissection protocol[8]. In short, the ear was surgically removed and affixed to a custom
493 3D-printed dish a custom-made 3D-print plastic dish, positioning the tympanum over a 3 mm
494 hole. For all measurements, the external side of the tympanum faced the sound source, while
495 the internal side, including Müller's organ, was submerged in locust extracellular saline. The
496 extracellular saline contained 185 mM NaCl, 10 mM KCl, 2 mM $MgCl_2$, 2 mM $CaCl_2$, 10 mM
497 HEPES, 10 mM trehalose, and 10 mM glucose. The pH was adjusted to 7.2 using NaOH.

498

499 **Sample preparation for FIB-SEM and 3D reconstruction of a scolopidium**

500 Excised locust ears were fixed in a solution of 2.5% glutaraldehyde and 2%
501 paraformaldehyde in 0.1 M sodium cacodylate (pH 7.2) with 4.1% sucrose. After washing, the
502 samples were incubated in 1% osmium tetroxide with 1.5% potassium ferricyanide, followed
503 by another wash and a 20-minute incubation in thiocarbohydrazide. Samples were then washed
504 and sequentially incubated in 2% aqueous osmium tetroxide and 2% uranyl acetate, with
505 washing steps in between. Following fixation and staining, the samples underwent serial
506 dehydration in ethanol (30%, 50%, 70%, 90%, and 100%). The samples were then washed in
507 propylene oxide before being embedded in a mixture of hard-formula TAAB 812 resin and
508 propylene oxide. The resulting resin blocks were trimmed to the region of interest, which was
509 verified by staining 100 nm-thick sections with methylene blue and imaging them on an
510 ultramicrotome (Leica UC7).

511 Serial imaging was performed on a dual-beam FIB-SEM (Zeiss Crossbeam 500) equipped
512 with a Gemini2 SEM column and a Ga^+ source. Imaging parameters were set as follows: SEM
513 extra high tension (EHT) at 1.6 kV with a 600 pA beam current, and FIB current at 700 pA at
514 30 kV. The voxel sizes of the acquired FIB-SEM stacks ranged from 9 to 15 nm. The 3D
515 ultrastructures of the scolopidia were reconstructed from the FIB-SEM stacks using image
516 processing software Dragonfly 3D.

517

518 **Optical Coherent Tomography Vibrometry**

519 We measured sound-evoked vibrations using a spectral domain Optical Coherence
520 Tomography (OCT) system (Ganymede, Thorlabs). The field of view was 10 × 10 mm with a
521 depth range of 3.5 mm. The OCT beam was directed from above, while the preparation was
522 mounted either horizontally (with the sound source below, Fig. 3a) or vertically (with the sound
523 source to the side, Fig. 3b). The beam was manually aligned for each measurement axis to
524 maximize the signal-to-noise ratio for that orientation. Sound stimuli, consisting of broadband
525 multitone "zwuis" complexes, were generated using a Tucker-Davis Technologies System III
526 and delivered via a ScanSpeaker R2904/700 005 loudspeaker, placed at 32 cm from the
527 preparation. The stimulus level was 90 dB SPL; based on previous work, this level in a liquid-
528 backed preparation corresponds to approximately 70 dB SPL in an air-backed tympanum[47].

529 OCT acquisitions were externally triggered and phase-locked to the acoustic stimulation
530 at a sampling rate of 90 kHz. To characterize the organ's complex 3D motion, vibrations were
531 measured separately along two primary axes: antero-posterior (motion normal to the tympanic
532 surface) and meso-lateral (tangential, side-to-side motion). Vibration waveforms were derived
533 from contiguous groups of three pixels per scan. All organ vibrations were measured relative
534 to the motion of the tympanum, which served as the phase and amplitude reference. The
535 significance of phase-locking for each frequency component was assessed using the Rayleigh
536 test ($p = 0.001$). All data acquisition and analysis were performed using a custom MATLAB
537 toolbox (MathWorks, 2007) developed by Marcel van der Heijden.

538

539 **Localisation of Group-III scolopidia**

540 To prepare the locusts for neural tracing, each insect was secured on its back in plasticine. A
541 small section of the cuticle on the second and third thoracic segments was carefully cut and
542 temporarily removed. After clearing away the tracheal air sacs to expose the metathoracic
543 ganglia and the auditory nerve (nerve VI), the thoracic cavity was filled with a saline solution.
544 The auditory nerve was then severed near the ganglion, and the cut end was positioned on the
545 outer cuticle at the rear of the thorax. A small well was made around the exposed nerve ending
546 using petroleum jelly and filled with a 5% Neurobiotin solution to allow the tracer to be
547 absorbed into the nerve. The well was sealed with more petroleum jelly, and the previously
548 removed cuticle was placed back onto the original area and also sealed to prevent the area from
549 drying out. The locusts were then incubated overnight at 4°C to facilitate the diffusion of
550 Neurobiotin along the auditory neurons. After the incubation, the locust ears were dissected
551 from the first abdominal segment. These ears were fixed in a 4% paraformaldehyde solution

552 for 24 hours at 4°C. Subsequently, the fixed ears were washed three times in Phosphate Buffer
553 Saline (PBS). To prepare for imaging, the ears were treated to make the cells permeable and to
554 block non-specific binding. They were then incubated overnight with Dylight 488 streptavidin,
555 which binds to the Neurobiotin to stain the auditory neurons, and DAPI, which stains the cell
556 nuclei. Finally, after another series of washes in PBS, the ears were dehydrated using an ethanol
557 series and cleared with Methyl salicylate. The stained neurons were then imaged using a
558 confocal microscope.
559 The positions of dendrite dilations were then manually registered in Fiji[48]. The positions
560 were recorded and saved as the region of interest (ROI) files and further processed in MATLAB
561 R2004a (Mathworks). The position of each dendrite dilation was computed as a relative
562 distance between the ganglion and the styliform body (Extended Data Fig. 2).
563
564 **Tracking sound-evoked scolopidium motion**
565 We recorded the sound-evoked motion of the scolopidium using a high-speed camera
566 (KINETIK, Teledyne) mounted on an FN1 Nikon upright microscope using a 40X/0.8W (NIR
567 Apo DIC N2) objective. We achieved an average acquisition rate of 8,602 ± 289 frame per
568 second (24 movies). The movie with acquisition rate that does not achieve Nyquist sampling
569 of its stimulated frequency were exclude from analysis. Sound stimulation was synchronised
570 with imaging and delivered through a speaker (RS PRO 50 mm, RS PRO) via an analogue-to-
571 digital converter (National Instruments PCIe 6323). The sound pressure level was calibrated
572 by measuring the voltage output of an amplified microphone (Clio PRE-01 and Clio MIC-03,
573 Audiomatica) in response to a 94 dB SPL 1 kHz tone from a sound level calibrator (Cal73,
574 Brüel & Kjær). This calibration allowed us to determine the sound pressure level from the
575 microphone's voltage output. The microphone was then positioned where the excised locust
576 ear would be during experiments, and speaker voltages were adjusted to produce a flat response
577 across the stimulated frequency range (1–5 kHz). An in-house MATLAB graphical user
578 interface controlled the setup. In these experiments, we stained the excised locust ear
579 preparation with 0.1% Janus Green B (201677-5G, Sigma Aldrich) to enhance the contrast of
580 the scolopidium with its surrounding tissue.
581 The sub-pixel resolution motion of the scolopidium were tracked using Fiji/ImageJ
582 Template Matching plugin (https://sites.google.com/site/qingzongtseng/template-matching-ij-
583 plugin)[49]. The tracking method is based on Normalised Correlation Coefficient and Gaussian
584 peak fitting to localise the location of the correlation peak. The coordinates output from the
585 plugin were further analysed in MATLAB R2004a (Mathworks).

586

587 **Whole-cell patch clamp and mechanical stimulation of a scolopidium**

588 To expose Group-III auditory neurons for patch-clamp recordings, the fibrous tissue enclosing
589 the medial–dorsal border of Müller's organ was digested by applying a solution of collagenase
590 (0.5 mg/ml) and hyaluronidase (0.5 mg/ml; C5138 & H2126, Sigma-Aldrich) in extracellular
591 saline. The enzymes were applied locally using a wide-bore (12 µm) patch pipette, which was
592 also used to gently remove the softened tissue via suction, exposing the somatic membrane of
593 the neurons.

594 To prepare for mechanical stimulation, the cap of a targeted scolopidium was released from
595 its attachment cell by puffing saline from a separate wide-bore pipette. The same pipette was
596 then used to hold the cap via gentle, continuous mouth suction, which was renewed
597 approximately every minute to ensure a secure connection. A series of push-pull (axial) and
598 up-down (normal) step displacements (1, 5, 10, 50, 100, 500, 1000, and 2000 nm) were
599 delivered to the stimulating pipette using a PatchStar micromanipulator (Scientifica).

600 Scolopidia were visualized with a custom upright microscope (Cerna® Mini, Thor Labs)
601 equipped with a 40× water-immersion objective (0.8 NA, 2 mm working distance; CFI APO
602 NIR, Nikon). Patch-clamp electrodes (3-4 MΩ) were fabricated from borosilicate glass
603 (GB150–8P, Science Products) using a vertical pipette puller (PC-100, Narishige). The
604 intracellular (pipette) solution contained (in mM): 170 K-aspartate, 4 NaCl, 2 MgCl2, 1 CaCl2,
605 10 HEPES, 10 EGTA, and 20 tetraethylammonium (TEA). The extracellular saline contained
606 (in mM): 185 NaCl, 10 KCl, 2 MgCl2, 2 CaCl2, 10 HEPES, 10 trehalose, 10 glucose, and 0.09
607 tetrodotoxin (TTX) citrate. To isolate and increase the magnitude of the transduction current,
608 spikes were blocked using extracellular TTX and intracellular TEA. Electrophysiological
609 signals were amplified, digitized, and recorded using an EPC 10 USB patch-clamp amplifier
610 (HEKA Elektronik).

611 Scolopidia were visualised with an upright microscope (Custom Cerna® Mini Microscope,
612 Thor Labs) using a water-immersion objective (40×, 0.8 numerical aperture, 2 mm working
613 distance; CFI APO NIR, Nikon). Electrodes with tip resistances ranging from 3 to 4 MΩ were
614 fabricated from borosilicate glass (inner diameter, 0.86 mm; GB150–8P, Science Products)
615 using a vertical pipette puller (PC-100, Narishige). Recording pipettes were filled with
616 intracellular saline containing the following (in mm): 170 K-aspartate, 4 NaCl, 2 MgCl2, 1
617 CaCl2, 10 HEPES, 10 EGTA, and 20 mm tetraethylammonium (TEA). The extracellular saline
618 contained the following in mM: 185 NaCl, 10 KCl, 2 MgCl2, 2 CaCl2, 10 HEPES, 10 trehalose,
619 10 glucose, and 90 tetrodotoxin (TTX) citrate. Spikes were blocked through extracellular TTX

620 and intracellular (pipette) TEA to increase the magnitude of the transduction current. The
621 electrophysiological measurements were amplified, digitised, and recorded using an EPC 10
622 USB patch-clamp amplifier (HEKA Elektronik).
623 The data analysis was done in MATLAB R2004a (Mathworks). Peak detections of the
624 ensemble average transduction current (Fig.5 f, g) were done by detecting peak within a 30-ms
625 windows at the onset of step-stimulation using Matlab built-in peak detection package
626 'findpeaks'.
627
628 **Statistical analysis**
629 Descriptive data are presented as the mean ± standard deviation. Biological replicates are
630 denoted by N (number of locusts), E (number of ears), and n (number of cells). For the
631 statistical analysis in Fig. 5j-m, we fitted linear regression models to assess the correlation
632 between the transduction current and the logarithmic step displacement (from 50-2000 nm). To
633 test for statistical differences, we performed a one-way ANOVA followed by Tukey's Honestly
634 Significant Difference (HSD) post-hoc test for multiple comparisons. The reported p-values
635 were obtained from the Tukey HSD procedure, while the t-statistics are from a Student's t-test.
636 Further details on the statistical analysis are available in the source data.
637
638 **Data availability**
639 Raw data and MATLAB codes supporting plots in this paper can be found in a public
640 repository. Source data for each figure are provided with this paper. Additional data can be
641 requested to the corresponding upon reasonable request.
642

643 **SUPPLEMENTARY INFORMATION**

644

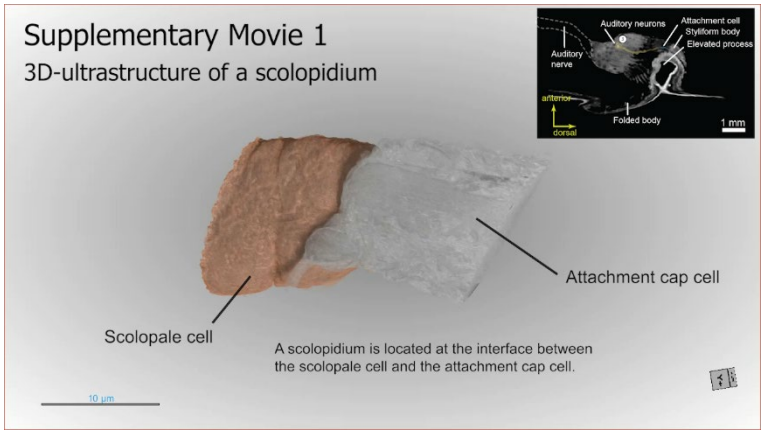

645

646 **SUPPLEMENTARY MOVIE 1.** The 3D ultrastructure of a scolopidium.

647

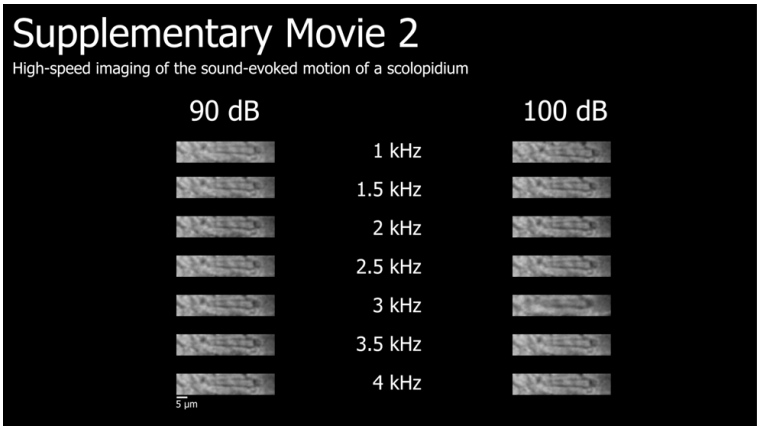

SUPPLEMENTARY MOVIE 2. High-speed imaging of the sound-evoked motion of the scolopidium.

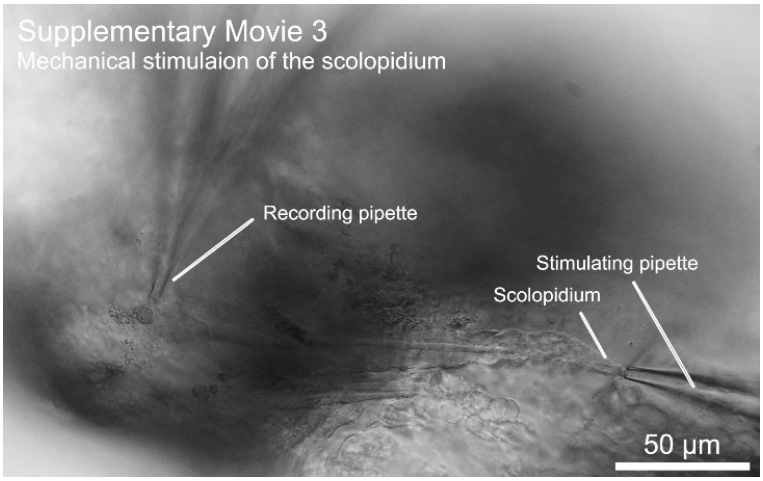

SUPPLEMENTARY MOVIE 3. Mechanical stimulation of the scolopidium cap. The movie is played at 18.75 frames per second.

655 **REFERENCES**

656 1. Warren, B. & Nowotny, M. Bridging the Gap Between Mammal and Insect Ears – A
657 Comparative and Evolutionary View of Sound-Reception. *Front. Ecol. Evol.* **9**, 667218
658 (2021).
659 2. Mendelson, M. The Site of Impulse Initiation in Bipolar Receptor Neurons of Callinectes
660 Sapidus L.*. *J. Exp. Biol.* **45**, 411–420 (1966).
661 3. Gray, E. G. The Fine Structure of the Insect Ear. *Philos. Trans. R. Soc. Lond. B. Biol. Sci.*
662 **243**, 75–94 (1960).
663 4. Field, L. H. & Matheson, T. Chordotonal Organs of Insects. in *Advances in Insect*
664 *Physiology* (ed. Evans, P. D.) vol. 27 1–228 (Academic Press, 1998).
665 5. Liang, X., Madrid, J., Saleh, H. S. & Howard, J. NOMPC, a member of the TRP channel
666 family, localizes to the tubular body and distal cilium of Drosophila campaniform and
667 chordotonal receptor cells. *Cytoskeleton* **68**, 1–7 (2011).
668 6. Li, B., Li, S., Zheng, H. & Yan, Z. Nanchung and Inactive define pore properties of the
669 native auditory transduction channel in Drosophila. *Proc. Natl. Acad. Sci. U. S. A.* **118**,
670 e2106459118 (2021).
671 7. Gong, Z. *et al.* Two Interdependent TRPV Channel Subunits, Inactive and Nanchung,
672 Mediate Hearing in Drosophila. *J. Neurosci.* **24**, 9059–9066 (2004).
673 8. Warren, B. & Matheson, T. The Role of the Mechanotransduction Ion Channel Candidate
674 Nanchung-Inactive in Auditory Transduction in an Insect Ear. *J. Neurosci.* **38**, 3741–3752
675 (2018).
676 9. Howse, P. The fine structure and functional organization of chordotonal organs. in *Symp*
677 *Zool Soc Lond* vol. 23 167–198 (1968).
678 10. Young, D. & Pringle, J. W. S. The structure and function of a connective chordotonal
679 organ in the cockroach leg. *Philos. Trans. R. Soc. Lond. B Biol. Sci.* **256**, 401–426 (1997).

11. Moran, D. T., Varela, F. J. & Rowley, J. C. Evidence for active role of cilia in sensory transduction. *Proc. Natl. Acad. Sci.* **74**, 793–797 (1977).

12. Thurm, U. An Insect Mechanoreceptor Part I: Fine Structure and Adequate Stimulus. *Cold Spring Harb. Symp. Quant. Biol.* **30**, 75–82 (1965).

13. Yang, J. *et al.* Rootletin, a novel coiled-coil protein, is a structural component of the ciliary rootlet. *J. Cell Biol.* **159**, 431–440 (2002).

14. Usherwood, P. N. R., Runion, H. I. & Campbell, J. I. Structure and Physiology of A Chordotonal Organ in the Locust Leg. *J. Exp. Biol.* **48**, 305–323 (1968).

15. Howse, P. E. & Claridge, M. F. The fine structure of Johnston's organ of the leaf-hopper, *Oncopsis flavicollis*. *J. Insect Physiol.* **16**, 1665–1675 (1970).

16. Whitear, M. & Medawar, P. B. The fine structure of crustacean proprioceptors I. The chordotonal organs in the legs of the shore crab, Carcinus maenas. *Philos. Trans. R. Soc. Lond. B. Biol. Sci.* **245**, 291–324 (1962).

17. Diakova, A. V. *et al.* The 3D ultrastructure of the chordotonal organs in the antenna of a microwasp remains complex although simplified. *Sci. Rep.* **12**, 20172 (2022).

18. Stephen, R. O. & Bennet-Clark, H. C. The Anatomical and Mechanical Basis of Stimulation and Frequency Analysis in the Locust Ear. *J. Exp. Biol.* **99**, 279–314 (1982).

19. Hummel, J. *et al.* Gating of Acoustic Transducer Channels Is Shaped by Biomechanical Filter Processes. *J. Neurosci. Off. J. Soc. Neurosci.* **36**, 2377–2382 (2016).

20. Vavakou, A., Scherberich, J., Nowotny, M. & van der Heijden, M. Tuned vibration modes in a miniature hearing organ: Insights from the bushcricket. *Proc. Natl. Acad. Sci.* **118**, e2105234118 (2021).

21. Michelsen, A. The physiology of the locust ear: I. Frequency sensitivity of single cells in the isolated ear. *Z. F*$\hat{u}$*r Vgl. Physiol.* **71**, 49–62 (1971).

22. Jacobs, K., Otte, B. & Lakes-Harlan, R. Tympanal receptor cells of Schistocerca gregaria: Correlation of soma positions and dendrite attachment sites, central projections and physiologies. *J. Exp. Zool.* **283**, 270–285 (1999).

23. Haskell, P. T. The influence of flight noise on behaviour in the Desert Locust *Schistocerca gregaria* (Forsk.). *J. Insect Physiol.* **1**, 52–75 (1957).

24. Wolfrum, U. Actin filaments: the main components of the scolopale in insect sensilla. *Cell Tissue Res.* **261**, 85–96 (1990).

25. Shanbhag, S. R., Singh, K. & Naresh Singh, R. Ultrastructure of the femoral chordotonal organs and their novel synaptic organization in the legs of *Drosophila melanogaster* Meigen (Diptera : Drosophilidae). *Int. J. Insect Morphol. Embryol.* **21**, 311–322 (1992).

26. Yack, J. E. & Roots, B. I. The metathoracic wing-hinge chordotonal organ of an atympanate moth, Actias luna (Lepidoptera, Saturniidae): a light- and electron-microscopic study. *Cell Tissue Res.* **267**, 455–471 (1992).

27. Michelsen, A. The physiology of the locust ear: II. Frequency discrimination based upon resonances in the tympanum. *Z. Für Vgl. Physiol.* **71**, 63–101 (1971).

28. Michelsen, A. The physiology of the locust ear: III. Acoustical properties of the intact ear. *Z. Für Vgl. Physiol.* **71**, 102–128 (1971).

29. Windmill, J. F. C., Bockenhauer, S. & Robert, D. Time-resolved tympanal mechanics of the locust. *J. R. Soc. Interface* **5**, 1435–1443 (2008).

30. Blockley, A., Ogle, D., Woodrow, C., Montealegre-Z, F. & Warren, B. Physiological changes throughout the ear due to age and noise - a longitudinal study. Preprint at https://doi.org/10.1101/2021.11.25.470017 (2021).

31. Hill, K. G. The physiology of locust auditory receptors. *J. Comp. Physiol.* **152**, 483–493 (1983).

729 32. Moran, D. T. & Carter Rowley, J. The fine structure of the cockroach subgenual
730 organ. *Tissue Cell* **7**, 91–105 (1975).
731 33. Bell, A. The pipe and the pinwheel: is pressure an effective stimulus for the 9+0
732 primary cilium? *Cell Biol. Int.* **32**, 462–468 (2008).
733 34. Wolfrum, U. Centrin- and α-actinin-like immunoreactivity in the ciliary rootlets of
734 insect sensilla. *Cell Tissue Res.* **266**, 231–238 (1991).
735 35. Mill, P. J. *Structure and Function of Proprioceptors in the Invertebrates*. (London :
736 Chapman and Hall, 1976).
737 36. Ravenscroft, T. A., Jacobs, A., Gu, M., Eberl, D. F. & Bellen, H. J. The Voltage-
738 Gated Sodium Channel in Drosophila, Para, Localizes to Dendrites As Well As Axons in
739 Mechanosensitive Chordotonal Neurons. *eNeuro* **10**, (2023).
740 37. Jin, P. *et al.* Cryo-EM Structure of the Mechanotransduction Channel NOMPC.
741 *Nature* **547**, 118–122 (2017).
742 38. Wang, Y. *et al.* The push-to-open mechanism of the tethered mechanosensitive ion
743 channel NompC. *eLife* **10**, e58388.
744 39. Duan, J. & Song, C. Twist is the key to the gating of mechanosensitive ion channel
745 NOMPC. *eLife* **13**, (2024).
746 40. Hehlert, P. *et al.* NOMPC ion channel hinge forms a gating spring that initiates
747 mechanosensation. *Nat. Neurosci.* **28**, 259–267 (2025).
748 41. Zhang, W. *et al.* Ankyrin Repeats Convey Force to Gate the NOMPC
749 Mechanotransduction Channel. *Cell* **162**, 1391–1403 (2015).
750 42. Howard, J. & Bechstedt, S. Hypothesis: A helix of ankyrin repeats of the NOMPC-
751 TRP ion channel is the gating spring of mechanoreceptors. *Curr. Biol.* **14**, R224–R226
752 (2004).

43. Howard, J. & Hudspeth, A. J. Compliance of the hair bundle associated with gating of mechanoelectrical transduction channels in the Bullfrog's saccular hair cell. *Neuron* **1**, 189–199 (1988).

44. Vavakou, A., Scherberich, J., Nowotny, M. & van der Heijden, M. Tuned vibration modes in a miniature hearing organ: Insights from the bushcricket. *Proc. Natl. Acad. Sci.* **118**, e2105234118 (2021).

45. Mhatre, N. *et al.* Reconstruction of sound driven, actively amplified and spontaneous motions within the tree cricket auditory organ. 2021.11.14.468538 Preprint at https://doi.org/10.1101/2021.11.14.468538 (2021).

46. Boo, K. S. & Richards, A. G. Fine structure of scolopidia in Johnston's organ of female Aedes aegypti compared with that of the male. *J. Insect Physiol.* **21**, 1129–1139 (1975).

47. Warren, B., Fenton, G. E., Klenschi, E., Windmill, J. F. C. & French, A. S. Physiological Basis of Noise-Induced Hearing Loss in a Tympanal Ear. *J. Neurosci. Off. J. Soc. Neurosci.* **40**, 3130–3140 (2020).

48. Schindelin, J. *et al.* Fiji: an open-source platform for biological-image analysis. *Nat. Methods* **9**, 676–682 (2012).

49. Tseng, Q. *et al.* A new micropatterning method of soft substrates reveals that different tumorigenic signals can promote or reduce cell contraction levels. *Lab. Chip* **11**, 2231–2240 (2011).